

# Automatic Left Atrial Appendage Orifice Detection for Preprocedural Planning of Appendage Closure

Walid Abdullah Al, Il Dong Yun\*, *Member, IEEE*, Eun Ju Chun

**Abstract—Objective:** In preoperative planning of left atrial appendage closure (LAAC) with CT angiography, the assessment of the appendage orifice plays a crucial role in choosing an appropriate LAAC device size and a proper C-arm angulation. However, accurate orifice detection is laborious because of the high anatomic variation of the appendage, as well as the unclear orifice position and orientation in the available views. **Methods:** We propose an automatic orifice detection approach performing a search on the principal medial axis of the appendage, where we present an efficient iterative algorithm to grow the axis from the appendage to the left atrium. We propose to use the axis-to-surface distance of the appendage for efficient and effective detection. To localize the necessary initial seed for growing the medial axis, we train an artificial localization agent using an actor-critic reinforcement learning approach, defining the localization as a sequential decision process. **Results:** The entire detection process takes only about 8 seconds, and the variance of the detected orifice with respect to annotations from two experts is calculated to be significantly small and less than the inter-observer variance. **Conclusion:** The proposed orifice search on the medial axis of the appendage comparing only its distance from the surface provides a simple, yet robust solution for orifice detection. **Significance:** While being the first fully automatic approach and providing a detection error below the inter-observer difference, our method improved the detection efficiency by eighteen times compared to the existing solution, therefore, can be potentially useful for physicians.

**Index Terms**—appendage closure, appendage occlusion, left atrial appendage, orifice detection, reinforcement learning

## I. INTRODUCTION

**A**TRIAL fibrillation (AF) characterized by rapid and irregular atrial beating is the most common among serious heart abnormalities [1]. According to the report by [2], AF affects 2–3% of the population, with a high increase comparing to 0.3–1% in 2005 [3]. The percentage rises with age affecting 14% of the population older than 80 years. One of the most prevalent sites of thrombus formation leading to AF-associated cardiovascular stroke is the left atrial appendage (LAA) [4]. LAA closure (LAAC) is a minimally invasive generalized treatment procedure gaining precedence over the risky anticoagulant (blood-thinning) medication [5]. It is an implant-based strategy to prevent the appendage clot from entering into the bloodstream, where the closure device is implanted through

a catheter. After the approval for WATCHMAN LAAC Implant by the U.S. in 2015, the adoption rate of this implant strategy for high-risk AF-patients is rising rapidly. For preoperative interventional planning, LAA assessment deserves due attention where the major concern to the physicians during the assessment is the detection of the orifice. Accurate estimation of the orifice parameters plays a significant role because it contributes to choosing the occlusion device of an appropriate size and obtaining a proper C-arm angulation for intervention.

Left atrial appendage can be viewed as an anatomical projection from the main left atrial chamber, and the LAA orifice (or, ostium) is the narrow opening of the appendage to the atrium. Surgical planning of LAAC utilizes CT angiography to acquire 3D measurements during the orifice assessment. However, significant variation in shape, size, and orientation of the appendage turns the assessment into a challenging problem. Moreover, conventional views do not allow a clear understanding of the appendage anatomy. In addition to the unclear LAA structure, the appendage and the left atrium also share a common intensity with no separation wall against each other. Consequently, accurate preprocedural assessment becomes laborious and time-consuming for the physicians. Therefore, an automatic approach for appendage orifice detection can be a great aid to the physicians by reducing their effort and speeding up the preoperative planning.

### A. Related works

With available LAA orifice assessment works strictly limited to manual approaches [6]–[8], the major research-focus is on the LAA segmentation where no indication is provided for the orifice. Prior segmentation approaches are also semi-automatic, usually requiring a manual volume-of-interest (VOI) annotation. Segmentation of LAA mostly comes together as a part of left atrium segmentation where LAA is included in the segmented left atrium without any distinction [9], [10]. A part-based segmentation approach proposed by [11], [12] suggests segmenting the whole left atrium by separate shape-constrained segmentation of six parts of the LA i.e., the LA chamber, four pulmonary veins (PVs), and the appendage, where the PV or appendage’s proximal ring projection toward the main chamber fills the inter-part gaps. However, such smoothed shape projection might fail to cope with the high variation of the orifice shape. Model-based approaches also face difficulty in segmenting near the tip of the LAA, presuming a smooth model for the complex lobe structure. Experimental results showed a higher error in case of the LAA comparing to the other parts [12].

Manuscript submitted on March 25, 2019. This research was supported by Basic Science Research Program through the National Research Foundation of Korea (NRF), funded by the Ministry of Education, Science, Technology (No. 2017R1A2B4004503).

W. A. Al and I. D. Yun are with the Department of Computer and Electronic Systems Engineering, Hankyong University of Foreign Studies, Yongin, South Korea. E. J. Chun is with the Department of Radiology, Seoul National University Bundang Hospital, Seongnam, South Korea.

(\*Correspondence email:yun@hufs.ac.kr)

With a few works treating the LAA segmentation as the major objective, Grasland-Mongarin et al. [13] presented a flexible model-based heart segmentation, where shape-constrained deformable models enable segmenting the cardiac chambers and the major vessels, and LAA was extracted using mesh inflation. The inflated model was able to cope with the varying shape of the LAA, however, segmentation near the tip was not satisfactory. Wang et al. [14] presented a semi-automatic non-model based method, where four fiducial points of the LAA are marked manually, followed by parametric max-flow enabled subsequent segmentation proposals for each 2D slice. A supervised forest regressor then elects the final 2D proposals for each slice, eventually merged to build the 3D segmented model. The approach of Jin et al. [15] also requires a manual selection of the VOI, where the subsequent 2D segmentation for the axial slices are obtained using fully convolutional networks (FCNs). A 3D conditional random field is then used to refine the 3D segmentation mask. Their approach could provide a satisfactory segmentation near the tip. However, such slice-wise prediction followed by 3D refinement is not efficient taking about 35 seconds excluding the manual marking. All these approaches include a part of the left atrium in their segmented model without presenting a clear separation or indication of the orifice.

Leventić et al. [16] propose a region growing-based segmentation from two manually annotated seed points (one in the LAA and the other in the LA outside the appendage). A separation plane is obtained from three additional points manually marked in the visualized segmented volume, representing the LAA ostium. Recently, they extended their work to compute the orifice location following a semi-automatic approach requiring a threshold to obtain initial mask and a seed-point in LAA [17]. Their approach starts with the LAA centerline extraction, which is based on a computationally expensive tracking of voxels with the maximum radius. At each step, the largest possible sphere around the current position is used as the search space for selecting the next maximum radii voxel in the initial mask. Furthermore, an additional skeletonization is performed to obtain the refined centerline from the tracked voxels. After performing LAA segmentation, the orifice-location is determined based on the cross-sectional area along the centerline. The optimal cross-section for each point in the centerline is determined by taking the minimum area given from multiple cross-sectional planes tilting the plane by up to 40 degrees. Overall, the whole process become computationally expensive taking about 2.5 minutes as reported in [17]. Moreover, the centerline may deviate to the adjacent left superior pulmonary vein (LSPV), which sometimes has a significant amount of leaking to the LAA. Determining the location of the orifice is also not sufficient for the preoperative planning of LAAC. The actual orifice plane and area should be detected for assessing the orifice parameters (e.g., diameter, area, angulation, etc.) in preoperative CT volume. ‘

## B. Contribution

In this paper, we propose a fully automatic approach to accelerate the LAA orifice assessment for LAAC by detecting

the orifice from the principal medial axis of the appendage. We show that the appendage axis-to-surface distance provides distinguishing information for accurate and efficient orifice detection. The proposed iterative medial axis growth algorithm is also efficient compared to the costly centerline tracking used by Leventić et al. [17], where we consider a small constant-sized search space to update to the next axial point. Inspired by the landmark localization by [18], we train a deep reinforcement learning (RL) agent to localize necessary seed for growing the medial axis. Where [18]’s approach learned the action-value function, we adopt the actor-critic method that performs a direct policy approximation for better convergence utilizing an additional value function to reduce the variance [19]. The proposed method showed a measurement error below the inter-observer difference while exhibiting robustness to patient-specific structural variation. The whole process takes only 8 seconds showing potential usefulness to be used in the clinical site. The contribution of our work can be summarized as follows:

- We propose the first fully automatic orifice detection and preprocedural assessment for LAAC, where we localize the LAA seed using a deep actor-critic RL agent.
- We propose to detect the orifice from the principal medial axis of the LAA. We also suggest an algorithm to grow the medial axis, which is significantly efficient compared with the centerline tracking used in the previous work [17].
- We show that using the appendage axis-to-surface distance information to detect the orifice-location can result in a more effective and efficient solution, instead of exhaustively searching for the optimum cross-sectional area at each axial point as used by Leventić et al. [17].
- In addition to the location of the orifice center, the actual orifice plane and area are also detected and validated CT volumes from 90 patients. The resultant orifice-parameters were compared against annotations from two different experts because orifice assessment has high interobserver variance.
- Taking only 8 seconds, the proposed automatic method is about eighteen times faster than the previous approach [17]. Resulting in an assessment-error below the inter-observer variance, the proposed orifice detection can be potentially useful for the physicians.

The rest of the paper is organized as follows. Section II presents the proposed method for automatic orifice detection. Section III presents the experimental results demonstrating the robustness and accuracy of the automatic assessment in CT angiography. Finally, Section IV discusses the concluding remarks.

## II. PROPOSED METHOD

The proposed automatic method starts with the seed localization required for the subsequent medial axis growth. An RL agent learns to localize the seed defined to be anywhere inside the appendage, by sampling consecutive actions from the learned parametrized policy. Using the geodesic distance from the localized seed, we extract the extended LAA volume.

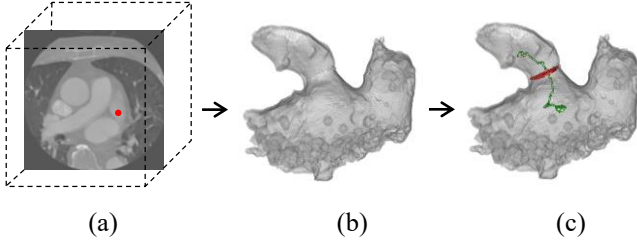


Fig. 1. **The proposed method for automatic orifice detection.** (a) Seed localization using RL. (b) Extended LAA extraction using geodesic distance relative to the seed. (c) Orifice detection from the corresponding principal medial axis, finding the axial point of maximum relative change in spatial distance map with respect to the surface. The green curve and red plane indicate the medial axis and the orifice, respectively.

Inside the extracted appendage, this seed then serves as the initial point for growing the principal medial axis, i.e., the search space for the orifice localization. Appendage axis-to-surface distance is then used to detect the orifice. Fig. 1 depicts the overall flow of our methodology. For a video illustration of the process, refer to the supplementary material. In the following, we present the description of each step in detail.

#### A. Seed Localization Agent

In the proposed method, the localization agent initiated at any random position  $\mathbf{x}_0$  inside the CT volume is allowed to take subsequent actions to move towards the target seed location  $\mathbf{x}_s$ . At any time  $t$ , the agent observes the corresponding state  $\mathbf{s}_t = \mathcal{S}(\mathbf{x}_t)$  for the current position  $\mathbf{x}_t$ . For the given state  $\mathbf{s}_t$ , the agent chooses an action  $a_t$  based on its optimal policy distribution  $\pi(\mathbf{s}_t, a_t)$ . By taking the optimal action  $a_t$ , it transitions to a new position  $\mathbf{x}_{t+1}$ . Going through an episode of such transitions, it eventually converges to  $\mathbf{x}_s$ . Thus, the localization process can be formulated as a Markov decision process (MDP) in RL. Fig. 2 schematically illustrates the localization for 2D case.

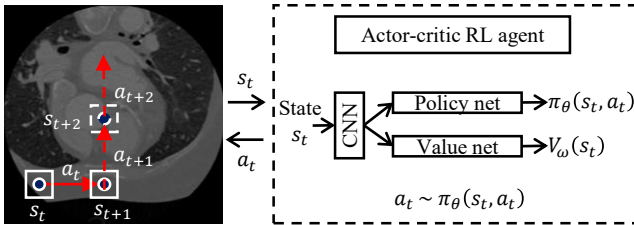


Fig. 2. **A 2D illustration of the seed localization process using actor-critic reinforcement learning agent.** At any time  $t$ , the agent observes the corresponding state  $\mathbf{s}_t$ , and chooses an action  $a_t$  based on the optimal policy distribution  $\pi_\theta$  for the current state, to move to any of the neighboring voxels. A sequence of such transitions enables the agent to reach the target seed position. The state is passed through a convolutional neural network before being fed to the policy and the value network. Policy network provides the optimal action probabilities for the current state, and the value network provides the approximated cumulative return for the current state. The value net is required only for reducing the variance during training and is not used during testing.

We obtain the state  $\mathcal{S}(\mathbf{x})$ , a function of the agent position  $\mathbf{x}$ , by concatenating the sagittal, coronal and axial sub-images centered at  $\mathbf{x}$ . The action-space  $\mathcal{A}$  simply includes six actions

referring to the positive and negative unit-steps along the 3D Cartesian axes. These actions allow the agent to move to any of the neighboring voxels considering a 6-connectivity. For a given state, the policy function  $\pi : \mathcal{S} \times \mathcal{A} \rightarrow [0, 1]$  gives the optimal action-probability. To learn the optimal policy, a supervised reward signal is fed for encouraging moves towards the target during training. Denoting a transition by  $(\mathbf{x}, a, \mathbf{x}')$  for a move from position  $\mathbf{x}$  to  $\mathbf{x}'$  by taking action  $a$ , the corresponding reward  $r = \mathcal{R}(\mathbf{x}, a, \mathbf{x}')$  is as follows:

$$\mathcal{R}(\mathbf{x}, a, \mathbf{x}') = \text{sign}(\|\mathbf{x}_s - \mathbf{x}\|_2 - \|\mathbf{x}_s - \mathbf{x}'\|_2) \quad (1)$$

where  $\|\cdot\|_2$  represents the L2 norm. Thus, an experience is denoted by appending the earned reward to the corresponding state transition, i.e.,  $(\mathbf{s}, a, \mathbf{s}', r)$  where  $\mathbf{s} = \mathcal{S}(\mathbf{x})$  and  $\mathbf{s}' = \mathcal{S}(\mathbf{x}')$ .

An actor-critic based direct policy search is exploited to learn the optimal agent-behavior because it gives better convergence compared with the commonly used value-based search (e.g., deep Q-networks). Actor-critic also uses an additional value function to reduce the variance problem of pure policy search approaches. We use the state-value function  $V^\pi(\mathbf{s}) : \mathcal{S} \rightarrow \mathbb{R}$  that outputs the expected long-term cumulative return earnable through the given state  $\mathbf{s}$  following a policy  $\pi$ . Deep convolutional neural network (CNN) is well known to understand and extract discriminative features from images. Therefore, we parametrize the policy and value function using CNN, where the policy and value functions are defined as exclusive fully connected stacks preceded by a common convolutional layer stack. For a given state  $\mathbf{s}$ , the policy net  $\pi_\theta$  (also called the actor) gives the optimal softmax-probabilities for all six actions, and the value net  $V_\omega$  (also called the critic) gives a scalar value referring to the cumulative return for  $\mathbf{s}$  following  $\pi_\theta$ . Here,  $\theta$  and  $\omega$  share the parameters of the convolutional stack. Thus, updating any of the actor and critic nets also affects the CNN part.

Using a temporal difference (TD) learning framework [20], we learn the optimal agent behavior. For each transition, we compute the discounted cumulative return  $R_\gamma(\mathbf{s}, a, \mathbf{s}', r) = r + \gamma V_\omega(\mathbf{s}')$  where  $\gamma$  is the discount factor. The goal of the critic is to optimize the value parameters so that it can provide an approximation of the discounted return  $R_\gamma$  for a given policy. On the other hand, the actor-update follows the advantage  $A_\gamma(\mathbf{s}, a, \mathbf{s}', r) = R_\gamma(\mathbf{s}, a, \mathbf{s}', r) - V_\omega(\mathbf{s})$  for a given value. Therefore, the optimal policy and value parameters are defined as follows:

$$\begin{aligned} \hat{\theta} &= \arg \min_{\theta} \mathbb{E}_{(\mathbf{s}, a, \mathbf{s}', r)} [-A_\gamma(\mathbf{s}, a, \mathbf{s}', r) \log \pi_\theta(\mathbf{s}, a)] \\ \hat{\omega} &= \arg \min_{\omega} \mathbb{E}_{(\mathbf{s}, a, \mathbf{s}', r)} [(R_\gamma(\mathbf{s}, a, \mathbf{s}', r) - V_\omega(\mathbf{s}))^2] \end{aligned} \quad (2)$$

where  $(\mathbf{s}, a, \mathbf{s}', r)$  is sampled from the agent experience following  $\pi_\theta$ . For a test CT volume, the agent starts from a random position and sequentially updates its position by sampling actions using the learned policy  $\pi_{\hat{\theta}}$  eventually converging to the target seed location.

#### B. Extended LAA extraction

Extracting the LAA volume is necessary for determining the principal medial axis and therefore detecting the orifice. The

extraction should be extensive in nature so that the resultant region includes a significant part of the left atrium beyond the appendage orifice. Otherwise, the following detection using the axis-to-surface distance can be ambiguous (which is discussed more in the following subsection). Existing LAA segmentation techniques could be used for appendage extraction. However, as discussed in the prior works subsection, the model-based approaches among those has the problem of coping with structural variation. The supervised slice-wise mask prediction comes with a large computational cost. Supervised approaches also requires marking the ground truth for 3D segmentation mask for all the training volumes. In contrast, we adopt a model-free 3D geodesic distance based unsupervised approach. In our case, supervised learning is not necessary because the LA and LAA has an even and easily distinguishable intensity distribution compared with the background. The only problem is the inclusion of left superior pulmonary vein (LSPV) as it also has similar intensity distribution. However, this does not affect our detection as we show in the following section. Obtaining the desired region directly from 3D geodesic distance instead of 2D slice-wise prediction enables a faster computation.

First, we obtain a fixed-size VOI relative to the seed location, so that it sufficiently encloses the appendage and a part of the LA. This may also include the LSPV. Inside the VOI, we compute the geodesic distance for all the voxels with respect to the localized seed  $\mathbf{x}_s$ . Finally, we can extract the extended LAA by thresholding the distance.

For a reference voxel-set  $\Omega$ , the geodesic distance at  $\mathbf{x}$  is defined as follows:

$$\begin{aligned} \mathcal{D}(\mathbf{x}; \Omega) &= \min_{\mathbf{y} \in \Omega} d(\mathbf{x}, \mathbf{y}) \\ d(\mathbf{x}, \mathbf{y}) &= \min_{\zeta \in \mathcal{P}_{\mathbf{x}, \mathbf{y}}} \sum_{\mathbf{p} \in \zeta} \sqrt{(\alpha^2 |\nabla_{\zeta} \mathbf{p}|^2 + (1 - \alpha)^2 |\nabla_{\zeta} I(\mathbf{p})|^2)} \end{aligned} \quad (3)$$

where  $\zeta$  iterates over all paths from  $\mathbf{x}$  to  $\mathbf{y}$ ,  $\mathcal{P}_{\mathbf{x}, \mathbf{y}}$ , and  $\nabla_{\zeta}$  indicates the gradient following a path  $\zeta$ .  $I$  denotes the intensity.  $\alpha$  sets the significance of spatial distance over intensity difference. Here,  $\Omega = \{\mathbf{x}_s\}$  contains the localized seed. Such geodesic distance is also used by Criminisi et al. [21] for segmentation. As opposed to the usual segmentation labelling decided by the comparative closeness to a foreground or background seed, a distance threshold parameter  $\lambda$  decides the segmentation in our case of a single foreground seed.

We compute the geodesic distance following the raster scan update scheme used by [21]. Two sets of forward and backward updates are performed. In the forward update, we visit and update each voxel using *upper-lower slice, top-bottom, left-right* scanning. Backward scan follows the opposite direction. The current voxel is updated using the geodesic distance information of its neighbours that have been visited in the current scan.

### C. Medial axis growth and orifice detection

The proposed principal medial axis refers to a branchless path from the appendage through the LAA neck to the LA beyond the orifice, and the orifice is detected based on the

distance of the axial points from the nearest surface. However, the usual medial axis transformation results in a path with junctions. To enable a single path axis from LAA to the LA, we define an energy function  $\mathcal{E}$  using the spatial distance transform relative to the nearest background and initiate a greedy walker at the seed location  $\mathbf{s}$ , moving towards a higher energy level stepping into unvisited neighboring voxels. Moreover, to avoid a walk towards a substructure before the atrium, a supervised trend vector  $\mathbf{t} \in \Phi^3$  (where  $\Phi = \{-1, +1\}$ ) defined as the signs of the difference from LAA tip to LA, is incorporated into the energy function. This trend vector forces the walker to follow the LAA to LA direction even if an unvisited voxel with higher energy level exists. The spatial distance transform  $\hat{\mathcal{D}}$  can be obtained using only spatial weighting in (3), i.e.,  $\hat{\mathcal{D}}(\mathbf{x}) = |\mathcal{D}(\mathbf{x}; \Omega_B)|_{\alpha=1}$ . Here,  $\Omega_B$  is the set of background voxels. For a voxel  $\mathbf{x}$ , the trend-embedded energy function of a neighboring voxel  $\mathbf{p}$  is defined as follows:

$$\mathcal{E}(\mathbf{p}; \mathbf{x}, \hat{\mathcal{D}}, \mathbf{t}) = \hat{\mathcal{D}}(\mathbf{p}) \text{sign}(\mathbf{t} \cdot (\mathbf{p} - \mathbf{x}) + c) \quad (4)$$

Here,  $c$  is the relaxation constant reducing the force to follow the trend. For example,  $c = 2$  encourages a step even if only one axial component of the update agrees with the trend. After performing  $T$  such steps with the walker, we obtain the desired medial axis path,  $\mathcal{M}$ . In our experiment, number of steps  $T$  was constant across all the volumes. Using the energy function in (4), Algorithm 1 presents the iterative position update to grow the principal medial axis.

The resultant medial axis serves as the search space for the orifice detection. Anatomy of the left atrial appendage suggests a gradually increased cross-sectional area from the LAA orifice to the LA unlike the area from LAA tip to the orifice. Instead of computing the cross-sectional area about the computed axial points in  $\mathcal{M}$ , we use the axis-to-surface distance (i.e., the distance of the axial points to the nearest surface) because it renders equivalent information. Moreover, the axis-to-surface distance about an axial point  $\mathbf{x} \in \mathcal{M}$  can be obtained directly from  $\hat{\mathcal{D}}(\mathbf{x})$  without any further computation. The axial point with the maximum increase in distance is set as the orifice position. Thus, incorporating the relative distance change, we simply define the orifice position on the medial axis as follows:

$$\mathbf{x}_o = \arg \max_{\mathbf{x} \in \mathcal{M}} [\hat{\mathcal{D}}(\mathbf{x} + \Delta \mathbf{x}) - \hat{\mathcal{D}}(\mathbf{x})] - [\hat{\mathcal{D}}(\mathbf{x}) - \hat{\mathcal{D}}(\mathbf{x} - \Delta \mathbf{x})] \quad (5)$$

Because the initial position of the walker i.e., the localized seed position, may not necessarily be in the centerline of the LAA, the initial segment of the medial axis leads the walker through high gradients in the distance map before it reaches the centerline and stabilizes. However, this initial segment cannot affect our detection since we use relative distance change.

After determining the orifice position, we infer the initial orifice plane with norm equivalent to the tangent at the position on the medial axis, where the final orifice plane is obtained by small refinement to have a minimum cross-sectional area. However, the over-segmented pulmonary vein region may lie on the plane during the refinement. In area computation, this region is discarded by watershed transformation [22] along the

**Algorithm 1** Principal medial axis growth**Input.**

Distance transform  $\hat{D}$  of the VOI, trend vector  $\mathbf{t}$ , relaxation constant  $c$ , seed voxel  $\mathbf{x}_s$ , number of steps  $T$

**Output.**

Principal medial axis,  $\mathcal{M}$

**Initialization.**

$\mathcal{M} = \emptyset$

$\mathbf{x} \leftarrow \mathbf{x}_s$

**for**  $i = 1$  to  $T$  **do**

  Mark  $\mathbf{x}$  as visited

$N_{\mathbf{x}} \leftarrow$  Unvisited neighbors of  $\mathbf{x}$

$\mathbf{x}' = \arg \max_{\mathbf{p} \in N_{\mathbf{x}}} \mathcal{E}(\mathbf{p}; \mathbf{x}, \hat{D}, \mathbf{t})$

  Append  $\mathbf{x}'$  to  $\mathcal{M}$

$\mathbf{x} \leftarrow \mathbf{x}'$

**end for**

corresponding orifice plane, resulting in an exclusive orifice region.

### III. RESULTS AND DISCUSSION

We validated our proposed method of automatic LAA orifice detection using CT volumes from 90 patients, where manually-annotated orifice parameters were provided for 32 of those. Hence, these annotated 32 volumes were used as the test set for final evaluation while the remaining 58 volumes being treated as the training set. Manual orifice assessment has high inter-observer variance. Therefore, annotations from two expert observers from the corresponding clinical site were provided for the test volumes so that we could compare the detection results against the inter-observer variance. 10 patients from the test set actually underwent through the appendage occlusion procedure using the WATCHMAN device. The pixel spacing of the volumes ranges from about 0.3 to 0.5 mm, where the inter-slice spacing ranges from 0.45 to 0.50 mm. The patients were about  $67 \pm 8$  years old, about 36% of them being female. The proposed approach builds upon a progressive methodology where each step in the pipeline depends on the success of the previous. Therefore, we detail the performance for each step gradually, starting with LAA localization.

#### A. LAA localization

The proposed RL-agent localizes any point near the LAA tip without any specificity. Manual marking of the seed to provide the agent with the reward signal while training was also done in a rough manner. Thus, we define the localized point to be *satisfactory* if (i) it is inside the appendage, and (ii) it resides near the appendage tip before the neck of the LAA. (i) is important for the segmentation while (ii) contributing to an appropriate medial axis growth for orifice detection. If the point is after the neck (near the orifice), the change in surface-to-axis distance can be confusing to determine the orifice position. Fixing this evaluation criterion, we move to describing the experimental settings for the actor-critic RL-agent.

The CNN state encoder consisted of 4 convolutional layer units with ReLU activation, each having a following Max. Pooling layer. The final layer was flattened to obtain a state feature vector removing the spatial dimensions. Policy and value networks were simple fully connected stacks, respectively outputting the optimal action-probabilities and the state-value for a given state traversed through the CNN. The window size for the state was set to 50, resulting a state of dimension  $50 \times 50 \times 3$ . Initiating from different random positions, the agent gathered episodes of experience by acting on the training volumes using an initial random policy, and stored them into a experience replay memory of size  $1 \times 10^5$ . From the experienced transitions, randomly sampled minibatches were used to update the actor and critic networks (with the inclusive CNN) using stochastic gradient descent. A discount factor  $\gamma = 0.9$  and a learning rate of  $1 \times 10^{-6}$  were used. Inspired by the work of [23], we used a Bayesian exploration strategy to model uncertainty in choosing actions using a dropout layer, where the keep-probability was annealed from 0.1 to 1.0 over the iterations.

Using the above-mentioned evaluation criterion, we present two kinds of evaluation- (i) initial position-basis, and (ii) patient-basis. (i) refers to the localization performance with respect to different initial positions in a test volume. Evaluation of this kind is important because initial point is random and it is possible that the agent may fail to reach the target from certain initial positions. We observed that agent-positions converges when a successful arrival occurs, and divergence arises otherwise due to possibly unknown or exceptional state occurrence within the search path. Therefore, we evaluated the performance as the probability of successful convergence from different initial positions in a test volume. About 86% of the initial positions resulted in convergence to the desired location. To ensure successful localization in each patient, we repeated the localization process for different initial positions until the convergence condition is met. Doing so, we could achieve a 100% localization success for the test set. The average number of attempts required was  $1.26 \pm 0.75$  with a maximum of 5. Table I summarizes the overall localization performance.

#### B. Appendage extraction and orifice detection

For the extracted appendage, we could only perform qualitative evaluation because there was no segmentation ground truth from the experts. Only the orifice boundary was present in the expert-annotations. For the segmentation to be useful, the resultant mask must contain a part of left atrium along with the appendage. A  $250 \times 250 \times 200$  VOI (in voxels) was sufficient to accommodate the appendage along with the desired part of the atrium. The geodesic distance threshold parameter  $\lambda$  to obtain the segmentation mask was set to 0.1, considering the normalized voxel intensity range  $[0, 1]$ . The resultant segmentation mask could successfully include the appendage along with a part of the left atrium. The LSPV was also included due to having similar intensity distribution, indirect connection through the atrium and/or direct connection to the appendage. Fig. 3 depicts segmentation results of different cases.

TABLE I  
LAA localization performance.

	Initial position-basis		Patient-basis	
	Mean $\pm$ SD	Median	Mean $\pm$ SD	Median
Localization success (%)	86.1 $\pm$ 5.6	88.3	100.0 $\pm$ 0.0	100.0
No. of attempts*	-	-	1.26 $\pm$ 0.75	1

\*Number of localization attempts in a patient from different initial positions until convergence.

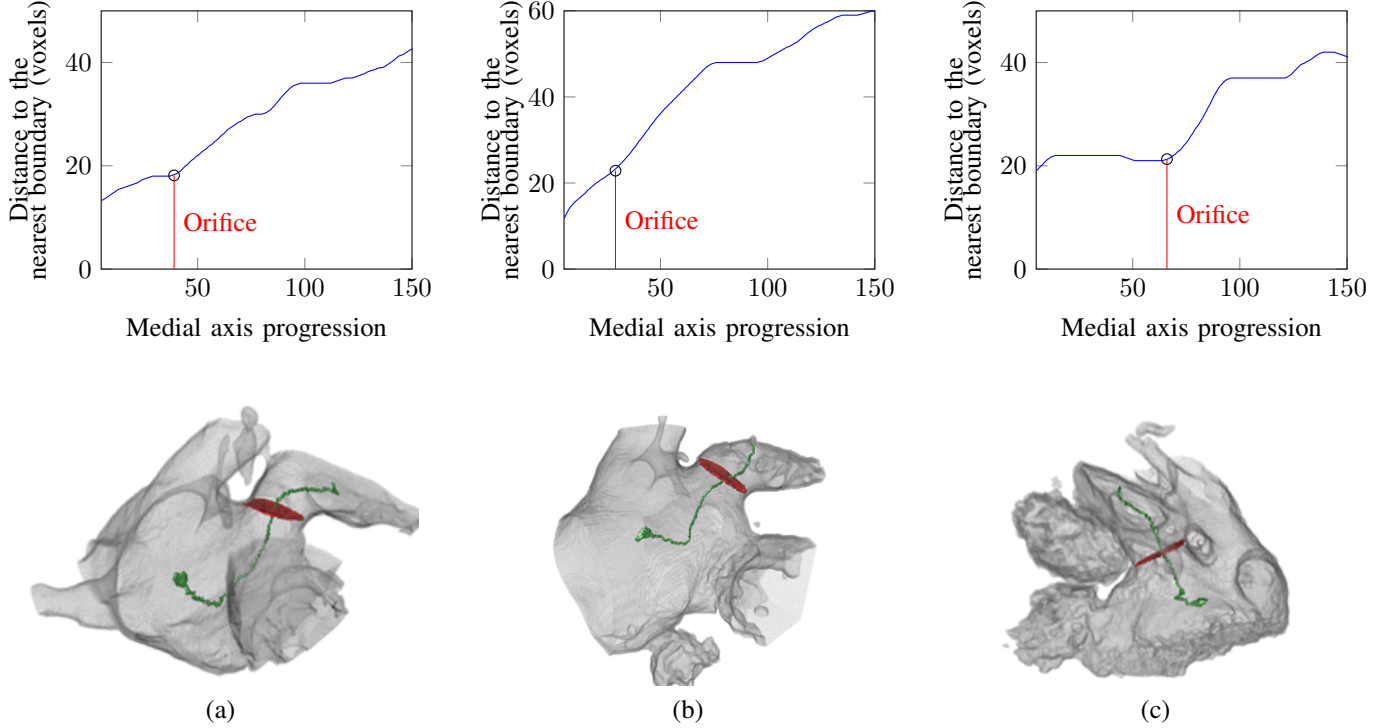


Fig. 3. **Orifice detection results.** (a) Localized seed is near the appendage centerline. (b) Localized seed is near the surface. The medial axis could eventually arrive the centerline by following the maximum distance to the surface in the proposed energy function. (c) The appendage has leaking through the LSPV and another adjacent organs. However, both the medial axis and orifice could be computed correctly.

From the localized position, the medial axis could also be grown successfully. The trend vector  $\mathbf{t}$  was obtained to be  $(-1, -1, 1)$ , which guided to grow the medial axis through the appendage neck towards the atrium, avoiding any possible deviation.  $T = 200$  position-updates were sufficient to grow the desired medial axis. The distance of the corresponding axial position to the nearest background was also stored. Such distance plot can be found in Fig. 3. The distance change rate was calculated for each axial position using a  $\Delta x = 5$  voxels. The position where maximum change occurs was chosen as the orifice position. Initial orifice plane (perpendicular to the medial axis tangent at the chosen orifice position), or the planes obtained during refinement may contain part of LSPV cross-section because LSPV can be present in the resultant segmentation mask. Fig. 4 depicts the exclusion of the LSPV in different cases by watershed segmentation.

We evaluated the finally detected orifice in terms of the parameters that are required for the WATCHMAN implantation (such as, average diameter, maximum diameter, minimum diameter, area, and perimeter). We also evaluated the orifice center and orientation. All the evaluation followed comparison with each of the expert observers. The inter-observer difference is also reported alongside. Table II presents

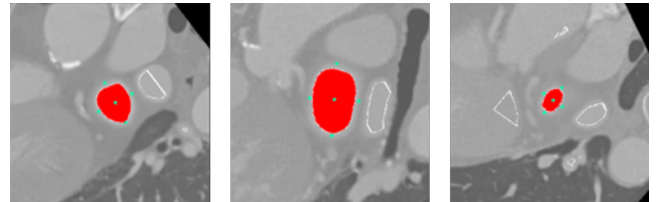


Fig. 4. **Exclusion of LSPV from orifice planes by watershed transformation.** White boundary is the resultant surface of extended LAA extraction. Watershed technique could successfully obtain the orifice part (filled with red color) from other undesired part that may be present in the original extraction. (Left and middle) partial and full inclusion of the LSPV in extracted region. (Right) partial inclusion of main pulmonary artery.

the absolute difference of the parameters obtained from the detected orifice with respect to the observers. Fig. 5 presents the overall error distribution for orifice center and diameter. For C-arm angulations (cranial/caudal and right/left anterior oblique (RAO/LAO) angles), signed error is presented.

The mean difference of the detected orifice center from the two-experts were only about  $2.49 \pm 1.38$  mm and  $2.28 \pm 1.18$  mm, respectively, whereas the difference of the previous approach [17] was reported to be  $2.51 \pm 2.97$  mm comparing

TABLE II  
ORIFICE DETECTION EVALUATION WITH RESPECT TO THE OBSERVERS.

Parameters	Ours/obs. 1	Ours/obs. 2	obs. 1/obs. 2
Orifice-center(mm)	$2.49 \pm 1.38$	$2.28 \pm 1.18$	$2.82 \pm 1.40$
Cranial/caudal angulation ( $^{\circ}$ )	$5.42 \pm 3.82$	$5.53 \pm 3.67$	$5.28 \pm 3.79$
RAO/LAO angulation ( $^{\circ}$ )	$6.62 \pm 4.49$	$5.19 \pm 3.70$	$6.07 \pm 4.06$
Avg. diameter (mm)	$1.67 \pm 1.53$	$1.62 \pm 1.28$	$2.55 \pm 1.53$
Min. diameter (mm)	$1.55 \pm 1.48$	$1.53 \pm 1.30$	$2.21 \pm 1.48$
Max. diameter (mm)	$1.72 \pm 1.60$	$1.58 \pm 1.43$	$3.40 \pm 1.79$
Area (mm <sup>2</sup> )	$2.27 \pm 1.94$	$2.01 \pm 1.37$	$5.31 \pm 2.03$
Perimeter (mm)	$5.34 \pm 4.93$	$5.03 \pm 4.15$	$8.17 \pm 5.06$

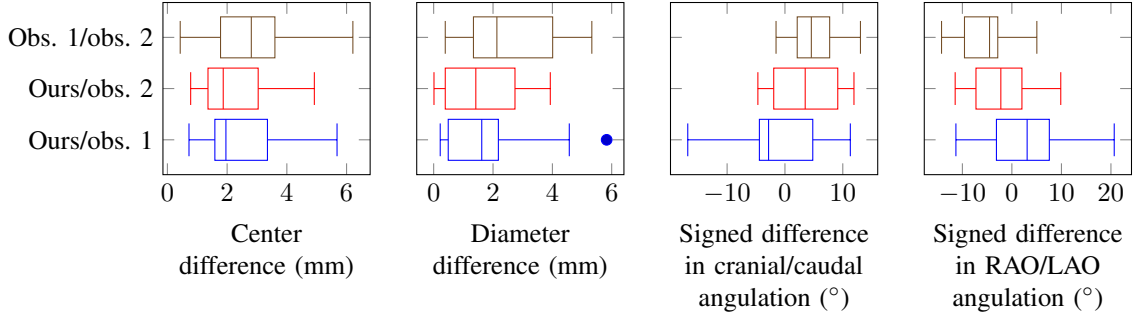


Fig. 5. **Box-plot of the detection error distribution compared with two observers.** The resultant orifice position, orientation, and diameter showed small variance from the expert observers.

against a single observer. The parameters required for choosing an appropriate size of WATCHMAN device showed a significantly small difference (with respect to each observer), which is below the inter-observer difference. For the 10 actual LAO patients, the average diameter differences were  $1.07 \pm 0.68$  mm and  $1.54 \pm 1.56$  mm with respect to the 1<sup>st</sup> and 2<sup>nd</sup> observer, where the inter-observer difference was  $2.19 \pm 1.69$  mm. The proposed automatic method is also notably efficient taking only about 8 seconds where a single-core 3.60 GHz CPU was used from segmentation to detection, and a GeForce Titan GPU was used for the RL-based localization. The repeatability test about the resultant diameter showed an error of  $0.78 \pm 0.63$  mm only. Therefore, we conclude that the proposed method being the first automatic orifice detection can potentially be useful for the physicians to accelerate the surgical planning of LAAC.

### C. Exceptional cases

For one test volume, we needed to reduce the segmentation threshold parameter  $\lambda$ . With the default threshold, an over-segmentation (that enters part of the boundary) was observed because the intensity difference between the appendage and the background was low. We had two failure cases, where the agent could not converge to the appendage at all. Even assigning the appendage seed manually, we could not detect the orifice because the segmentation and medial axis growth were also problematic. Fig. 6 shows the exceptional cases. The first case had a very narrow connection of appendage to the atrium. In the second case, we observed an uneven intensity distribution in the appendage, yielding problems in geodesic distance computation.

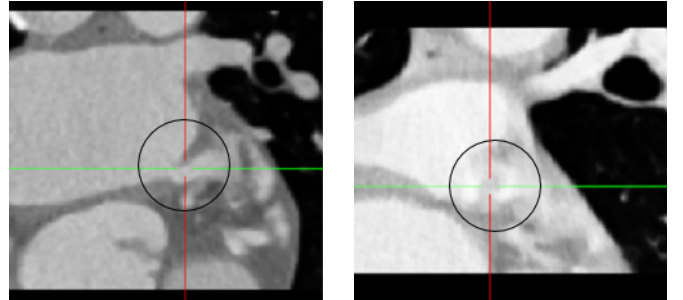


Fig. 6. **The two failure cases.** (Left) thin connection prevents the medial axis growth into the LA. (Right) distorted appendage intensity causes a problematic geodesic distance map.

## IV. CONCLUSION

We presented the first automatic method of appendage orifice detection in preoperative planning of appendage closure, where the orifice is detected from the principal medial axis of an extensively segmented LAA volume grown from an actor-critic reinforcement learning agent-localized seed. We validated our method by comparing the detected orifice parameters with manual annotations from two different experts. With a notable repeatability and efficiency, the proposed method showed significantly small error that is below the inter-observer variance. Taking only about 8 seconds, the proposed detection approach can potentially be useful for physicians to reduce their efforts and accelerate the planning.

## ACKNOWLEDGMENT

This research was supported by Basic Science Research Program through the National Research Foundation of Korea (NRF), funded by the Ministry of Education, Science, Technology (No. 2017R1A2B4004503).

## REFERENCES

- [1] M. TM, W. LQ, and S. WK, "Atrial fibrillation," *Biomedical Research*, vol. 28, no. 1, pp. 1–17, 2014.
- [2] M. Zoni-Berisso, F. Lercari, T. Carazza, and S. Domenicucci, "Epidemiology of atrial fibrillation: European perspective," *Clinical Epidemiology*, vol. 6, p. 213, 2014.
- [3] V. Fuster, L. Ryden, D. Cannom, H. Crijns, A. Curtis, K. Ellenbogen, J. Halperin, J. Le Heuzey, G. Kay, J. Lowe *et al.*, "American college of cardiology, american heart association and european society of cardiology (2006) guidelines for the management of patients with atrial fibrillation," *Rational Pharmacotherapy in Cardiology*, vol. 3, no. 2, pp. 72–97, 2015.
- [4] L. D. Burrell, B. D. Horne, J. L. Anderson, J. B. Muhlestein, and B. K. Whisenant, "Usefulness of left atrial appendage volume as a predictor of embolic stroke in patients with atrial fibrillation," *The American Journal of Cardiology*, vol. 112, no. 8, pp. 1148–1152, 2013.
- [5] D. R. Holmes Jr, S. K. Doshi, S. Kar, M. J. Price, J. M. Sanchez, H. Sievert, M. Valderrabano, and V. Y. Reddy, "Left atrial appendage closure as an alternative to warfarin for stroke prevention in atrial fibrillation: a patient-level meta-analysis," *Journal of the American College of Cardiology*, vol. 65, no. 24, pp. 2614–2623, 2015.
- [6] L. P. Budge, K. M. Shaffer, J. R. Moorman, D. E. Lake, J. D. Ferguson, and J. M. Mangrum, "Analysis of in vivo left atrial appendage morphology in patients with atrial fibrillation: a direct comparison of transesophageal echocardiography, planar cardiac CT, and segmented three-dimensional cardiac CT," *Journal of Interventional Cardiac Electrophysiology*, vol. 23, no. 2, pp. 87–93, 2008.
- [7] Y. Wang, L. Di Biase, R. P. Horton, T. Nguyen, P. Morhanty, and A. Natale, "Left atrial appendage studied by computed tomography to help planning for appendage closure device placement," *Journal of Cardiovascular Electrophysiology*, vol. 21, no. 9, pp. 973–982, 2010.
- [8] D. T. Walker, J. A. Humphries, and K. P. Phillips, "Anatomical analysis of the left atrial appendage using segmented, three-dimensional cardiac CT: a comparison of patients with paroxysmal and persistent forms of atrial fibrillation," *Journal of Interventional Cardiac Electrophysiology*, vol. 34, no. 2, pp. 173–179, 2012.
- [9] C. Tobon-Gomez, J. Peters, J. Weese, K. Pinto, R. Karim, T. Schaeffter, R. Razavi, and K. S. Rhode, "Left atrial segmentation challenge: a unified benchmarking framework," in *International Workshop on Statistical Atlases and Computational Models of the Heart*. Springer, 2013, pp. 1–13.
- [10] H. Liu, J. Feng, Z. Feng, J. Lu, and J. Zhou, "Left Atrium Segmentation in CT Volumes with Fully Convolutional Networks," in *Deep Learning in Medical Image Analysis and Multimodal Learning for Clinical Decision Support*. Springer, 2017, pp. 39–46.
- [11] Y. Zheng, M. John, J. Boese, and D. Comaniciu, "Precise segmentation of the left atrium in C-arm CT volumes with applications to atrial fibrillation ablation," in *IEEE International Symposium on Biomedical Imaging (ISBI)*. IEEE, 2012, pp. 1421–1424.
- [12] Y. Zheng, D. Yang, M. John, and D. Comaniciu, "Multi-part modeling and segmentation of left atrium in C-arm CT for image-guided ablation of atrial fibrillation," *IEEE Transactions on Medical Imaging*, vol. 33, no. 2, pp. 318–331, 2014.
- [13] P. Grasland-Mongrain, J. Peters, and O. Ecabert, "Combination of shape-constrained and inflation deformable models with application to the segmentation of the left atrial appendage," in *Biomedical Imaging: From Nano to Macro, 2010 IEEE International Symposium on*. IEEE, 2010, pp. 428–431.
- [14] L. Wang, J. Feng, C. Jin, J. Lu, and J. Zhou, "Left Atrial Appendage Segmentation Based on Ranking 2-D Segmentation Proposals," in *International Workshop on Statistical Atlases and Computational Models of the Heart*. Springer, 2016, pp. 21–29.
- [15] C. Jin, J. Feng, L. Wang, J. Liu, H. Yu, J. Lu, and J. Zhou, "Left atrial appendage segmentation using fully convolutional neural networks and modified three-dimensional conditional random fields," *IEEE Journal of Biomedical and Health Informatics*, 2018.
- [16] H. Leventic, D. Babin, L. Velicki, I. Galie, and V. Zlokolica, "Semi-automatic left atrial appendage segmentation from 3D CCTA images," in *2017 International Symposium ELMAR*. IEEE, 2017, pp. 39–42.
- [17] H. Leventić, D. Babin, L. Velicki, D. Devos, I. Galić, V. Zlokolica, K. Romić, and A. Pižurica, "Left atrial appendage segmentation from 3D CCTA images for occluder placement procedure," *Computers in biology and medicine*, vol. 104, pp. 163–174, 2019.
- [18] F. C. Ghesu, B. Georgescu, T. Mansi, D. Neumann, J. Hornegger, and D. Comaniciu, "An artificial agent for anatomical landmark detection in medical images," in *International Conference on Medical Image Computing and Computer-Assisted Intervention*. Springer, 2016, pp. 229–237.
- [19] R. S. Sutton, D. A. McAllester, S. P. Singh, and Y. Mansour, "Policy gradient methods for reinforcement learning with function approximation," in *Advances in Neural Information Processing Systems*, 2000, pp. 1057–1063.
- [20] V. Mnih, K. Kavukcuoglu, D. Silver, A. A. Rusu, J. Veness, M. G. Bellemare, A. Graves, M. Riedmiller, A. K. Fidjeland, G. Ostrovski *et al.*, "Human-level control through deep reinforcement learning," *Nature*, vol. 518, no. 7540, p. 529, 2015.
- [21] A. Criminisi, T. Sharp, and A. Blake, "Geos: Geodesic image segmentation," in *European Conference on Computer Vision*. Springer, 2008, pp. 99–112.
- [22] S. Beucher, "The watershed transformation applied to image segmentation," *Scanning Microscopy-Supplement*, pp. 299–299, 1992.
- [23] Y. Gal, J. Hron, and A. Kendall, "Concrete Dropout," in *Advances in Neural Information Processing Systems (NIPS)*, 2017.